DOI: 10.1002/ ((please add manuscript number))
Article type: Full Paper

Synthesis of In_2S_3 and In_6S_7 Microcolumns and Nanowires by a Vapor-Solid Method

Javier Bartolomé, David Maestre, and Ana Cremades*

Dedicated to Prof. Javier Piqueras

Dr. J. Bartolome, Dr. D. Maestre, Prof. Dr. A. Cremades
Departamento de Física de Materiales, Universidad Complutense de Madrid, Madrid, 28040, Spain
E-mail: j.bartolome@fis.ucm.es

Keywords: indium sulfide, In_2S_3, In_6S_7, nanowires, solar cells

Indium sulfide (In_2S_3) is a promising candidate for the replacement of CdS buffer layers in solar cell devices, while hexaindium heptasulfide (In_6S_7) presents interesting properties for its use as absorber material. In this work the fabrication of In_2S_3 microcolumns as well as novel In_6S_7 nanowires with diameters of about 70-120 nm is reported. The structures are grown following a thermal evaporation-deposition method at temperatures between 900 and 1000 ºC. Control of the phase and morphology of the structures is achieved through both the evaporation and deposition temperatures, which can be tuned separately. Energy dispersive spectroscopy shows no traces of residual oxygen, while X-ray photoelectron spectroscopy indicates the presence of small amounts of oxygen incorporated at the surface of the structures. The In_6S_7 nanowires are found to be degenerated n-type semiconductors, with the Fermi level above the conduction band minimum. The origin of this n-type degeneracy is discussed in terms of S vacancies.

1. Introduction

The In-S system has been extensively studied for several decades and it is currently of great interest due to its potential applications in optoelectronics and the solar cell industry. Several In-S based compounds have been reported in the literature such as In_2S_3, InS, $In_{3-x}S_4$ and In_6S_7.[1,2] Among them, indium sesquisulfide (In_2S_3) and hexaindium heptasulfide (In_6S_7) are

attracting an increasing interest in photovoltaics and as photodetectors. In_2S_3 is currently being investigated for replacing CdS buffer layers in high efficiency solar cell based on $CuInS_2$-In_2S_3 heterostructures.[3–6] The presence of three In_2S_3 polymorphic structures is also of interest to tailor the required material properties for different applications. Cubic α-In_2S_3 and trigonal γ-In_2S_3 phases are stable above 420 and 754 ºC respectively, although they can be stabilized at room temperature by incorporating an excess of In (α-phase) or doping with As or Sb (γ-phase).[7] Tetragonal β-In_2S_3 is the most studied In_2S_3 phase as it is stable at room temperature. It presents a defective spinel structure with an indirect bandgap of around 2.0 eV,[8,9] and behaves as an intrinsic n-type semiconductor due to the presence of S vacancies, with large photoconductivity responses.[10] It also presents a variable direct bandgap of 2.2 – 2.8 eV, which is strongly dependent on its growth conditions, stoichiometry and microstructure.[11,12] This variable bandgap can be exploited in the fabrication of solar cell window layers, in replacement of other wide bandgap materials. Oxygen incorporation into the indium sulfide lattice has been reported to have a positive effect as oxygen-containing layers exhibit properties matching the specifications of solar cell buffer layers.[13] Stoichiometric In_2S_3 is a highly resistive material which becomes conductive when oxygen replaces sulfur, despite widening its bandgap.[14] Nanostructuring of the surface has been used as a way to decrease the cell reflectivity and thus increase their energy conversion. Several studies have been reported on nanostructured In_2S_3 grown by different methods.[6,10,15–19]

Monoclinic hexaindium heptasulfide (In_6S_7) was first identified by Duffin and Hogg.[1,20] It belongs to the $P2_1/m$ space group, presents an intrinsic n-type conductivity[21] and, contrary to β-In_2S_3, has a direct bandgap usually reported in the range of 0.6-0.9 eV, although more accurate measurements estimated its value to be 0.93 eV.[22,23] Narrow bandgap materials are typically used in infrared related applications such as photodetectors; however they can also be used as absorbers in solar cells. Zdanowicz et al.[24] showed that narrow bandgap (~1 eV) single junction solar cells may have conversion efficiencies as high as 28% (compared to the

optimum 33%), while presenting reduced performance degradation under poor irradiation conditions, such as those usually present in the northern countries. Besides, the theoretical maximum efficiency of double junction cells is achieved when the low bandgap absorber is close to 1 eV, regardless of the irradiation or temperature conditions. Similarly, the advent of thermophotovoltaics has shifted the attention to narrower bandgap materials to efficiently absorb the infrared part of the spectrum in thermal waste recovery applications.[25] Typical materials used in this field are Si, GaSb, copper indium gallium diselenide (CIGS) or Ge, with bandgaps in a similar range as In_6S_7. Therefore In_6S_7 is a promising candidate as absorber material in the field of photovoltaics.[23,26] Moreover, this material has demonstrated photocatalytic activity under visible light irradiation.[27] However, despite its interest there are scarce reports on the physical properties of this material, which has been obtained mainly as single or polycrystalline bulk samples.

In this work we report the growth by a vapor phase deposition method of β-In_2S_3 columnar microcrystals and novel In_6S_7 nanowires. This method has been demonstrated to yield high density of elongated micro and nanostructures of different semiconductors without the use of a catalyst.[28–30] Control of the phase and morphology of the crystals is achieved by tuning the deposition temperature as well as the supersaturation of the evaporated precursors, which in turn is controlled through the pressure inside the furnace and the evaporation temperature at its center. Their morphological, structural and electronic properties are investigated by means of X-ray diffraction (XRD), energy dispersive spectroscopy (EDS) and X-ray photoelectron spectroscopy (XPS).

2. Experimental Section

In_2S_3 pellets, obtained by compaction of commercial powder (99.9 % purity, Sigma Aldrich), were used as the precursor, while ceramic In_2O_3 discs, obtained by oxidation of In_2S_3 pellets at 900 ºC in air, were employed for the deposition and growth of different In-S micro- and

nanostructures. The precursors were loaded into a sealed horizontal furnace with a base pressure of ~10^{-2} mbar, and heated at either 900 or 1000 ºC for 5 h under argon flow. The In_2O_3 substrates were located downstream from the precursor, in the low temperature region of the furnace. Two different substrates, separated 5 cm from each other, were used per treatment. The corresponding deposition temperatures were approximately 730 and 540 ºC for the treatment at 900 ºC, and 825 and 650 ºC for the treatment at 1000 ºC. A scheme of the experimental setup, as well as the temperature profile and sample location is shown in **Figure 1**. Samples are labeled according to the treatment temperature and location of the substrates (A or B), e.g. sample 900B (see Figure 1b). Composition and phase identification of the samples was performed by means of EDS with a Bruker AXS 4010 detector mounted on a Leica 440 scanning electron microscope (SEM), and XRD in both Bragg-Brentano and grazing incidence configurations employing a PANalytical's X'Pert MPD diffractometer. XPS measurements were performed at the ESCA microscopy beamline of the Elettra Synchrotron facilities, with a photon energy of 640 eV, and a resolution of 0.2 eV. The scanning photoelectron microscope can work with spatial resolution in the submicrometer range in both spectroscopy and imaging modes, enabling local XPS measurements to be obtained on individual micro- and nanostructures. Carbon 1s peak (284.4 eV) from residual carbon species was used as a reference for calibration of the peak positions in the XPS spectra.

3. Results and discussion

After the thermal treatments, a color change is observed in the originally yellow substrates due to the deposited material. In the case of the treatment performed at 900 ºC, both samples (900A and 900B) present a metallic dark gray color. XRD patterns recorded in Bragg-Brentano configuration indicates that sample 900A (the one closer to the precursor pellet) is covered by β-In_2S_3, with some traces of cubic In_2O_3 pertaining to the ceramic substrate, as revealed by comparison with standard JCPDS cards 03-065-0459 and 00-006-0416,

respectively (**Figure 2**a). On the other hand, sample 900B shows only the presence of In_2O_3 peaks from the substrate; however, when the setup configuration is changed to grazing incidence, a plethora of new peaks can be observed, revealing the existence of a deposited very thin layer of different composition (Figure 2b). These peaks cannot be attributed to either In_2O_3 or any of the conventional In_2S_3 or InS phases; instead they are identified as In_6S_7 (JCPDS card 01-072-0011), with contribution from the In_2O_3 substrate on the most intense peaks.

Figure 3 shows representative SEM images of the surface of both samples. The surface of sample 900A is essentially composed of small crystallites and large, faceted grains with triangular terraces. The corresponding In:S ratio measured by EDS is $r_{In:S}$ = 0.69 (Figure 4a), very close to stoichiometric In_2S_3 ($r_{In:S}$ = 0.67), in agreement with XRD results. Sample 900B, on the other hand, is covered by nanowires with diameters of 70 to 120 nm and lengths up to 10 µm. These nanowires can be present either individually (Figure 3b) or grouped together forming bundles like those shown in Figure 3c. A detail of the bundles, which present thicknesses of several microns, is shown in Figure 3d, where the composing single nanowires can be clearly distinguished. Typical In:S ratios of $r_{In:S}$ = 0.98-1.17 (**Figure 4**a) measured on the nanowires indicate an excess of In compared to the stoichiometric formula of In_6S_7 ($r_{In:S}$ = 0.86). Since no signal of metallic In was found by XRD it is suggested that the excess of In is actually a deficiency of S, which is a common characteristic of the In-S material system. No traces of residual O were found by EDS on any of the samples within the resolution limit of the technique.

For treatments performed at 1000 ºC each sample presented a different color. The substrate closer to the precursor (sample 1000A) maintained its yellow surface, indicative of an almost inexistent material deposition, except for a small region at the edge opposite to the precursor, which showed a dark reddish coloration. To differentiate both regions they will be hereinafter called samples O-1000A (yellow) and S-1000A (dark red), respectively. XRD measurements

performed on sample 1000A shows mainly peaks associated to In_2O_3, with a very small contribution from the most intense peaks of β-In_2S_3 (marked with a § symbol in Figure 2a), most likely coming from the reddish region S-1000A. This region is too small to be probed by XRD independently from the rest of the sample, however the contribution from β-In_2S_3 intensifies slightly when the beam is localized on it (Figure 2c), indicating the deposition of β-In_2S_3 at this region. The yellow area is formed by sintered grains and in some cases well faceted crystals with pyramidal or octahedral shapes are also developed as the one shown in the inset of **Figure 5**a. The reddish region on the other hand is covered by the same triangular terraces characteristic of sample 900A, intercalated with areas of sintered In_2O_3 grains and pyramids (Figure 5a). EDS measurements confirm that the surface of the (yellow) region O-1000A is essentially composed of In_2O_3, with no traces of sulfur, while the triangular terraces from S-1000A are composed of In_2S_3, with an In:S ratio of $r_{In:S}$ = 0.68, close to the stoichiometric value, and no residual O (Figure 4b).

Sample 1000B on the other hand presented a metallic dark gray color, similar to sample 900B, and it is mainly covered by In_6S_7, as evidenced from the XRD pattern (Figure 2a). SEM images show the formation of individual nanowires at the edge of the sample (Figure 5b), while the surface is totally covered by elongated grains (Figure 5c), which are the result of the coalescence of nanowire bundles, as evidenced from their grooved appearance. Measured In:S ratios of $r_{In:S}$ = 0.82 (Figure 4b) are close to the expected values for In_6S_7 ($r_{In:S}$ = 0.86), in agreement with XRD. The region closer to the gas inlet presents a different morphology, with triangular shaped column-like crystallites (Figure 5d and inset). This crystallites resemble those found on sample 900A and present In:S ratios of around $r_{In:S}$ = 0.71, closer to the In_2S_3 phase. Localized XRD measurements shows again intensified β- In_2S_3 peaks, confirming this composition.

Further investigation of the surface composition of the samples was performed by XPS. Measurements were carried out on representative regions of the three studied phases, namely samples 900B, 1000B, and the In_2O_3 and In_2S_3 rich regions of sample 1000A. XPS spectra of the In_2S_3 precursor powders were also obtained as reference. **Figure 6** shows the corresponding survey spectra, as well as the S (2p), In (3d), O (1s) core levels and valence band (VB) of the samples. All the peaks can be properly described by single component Voigt profiles except for the S (2p) core level, which is composed by two doublets in all cases. The main doublet is located at binding energies (BE) of approximately 161.7 eV ($2p_{5/2}$) and 163.0 eV ($2p_{3/2}$), while a weak component appears around 162.6 and 164.0 eV, as indicated by the dashed lines in Figure 6b. **Table 1** shows the obtained binding energies for all the studied core levels, as well as the Fermi level with respect to the VB maximum (E_F – VB). The binding energy of the main doublet of the S (2p) core level shows very small variations between different samples and corresponds to S bonded to In for all the samples, as reported by Tao et al.[31] (BE S($2p_{3/2}$) ~ 161.7 eV). The second contribution could be attributed to S deficient regions, similar to the photoemission process described by Fan and Goodenough[32] to explain the high energy component of the O (1s) core level in In_2O_3. Another possibility would be the formation of S-O bonds, however it can be ruled out since the binding energies of SO_x species are several eV higher than the values observed here.[33]

Contrary to the case of S (2p) core level, In (3d) (Figure 6c) shows appreciable shifts between the different samples. Reference In_2S_3 powders as well as the O-rich region of sample 1000A (O-1000A) present In ($3d_{5/2}$) binding energies close to the reported values for pure In_2S_3 (~444.9 eV)[29] and In_2O_3 (~444.7 eV),[32,33] respectively. For samples 900B and 1000B, on the other hand, the values are shifted towards higher binding energies, up to 0.57 eV compared to In_2O_3, and up to 0.20 eV with respect to In_2S_3. Besides no contribution from metallic In^0 (BE In ($3d_{5/2}$) ~ 443.8 eV) is observed on any of the samples, supporting the surface S deficiency evidenced by the presence of the second component in the S (2p) spectra, and in agreement

with the bulk S deficiency observed by EDS in sample 900B. The BE shift of samples 900B and 1000B can be attributed to the presence of In_6S_7 phase, in agreement with XRD and EDS measurements, although its exact origin is unclear. Chemical shifts are usually produced by a change in oxidation state of the element; however an increase in binding energy would be explained by an increase in oxidation state of In, while the opposite is expected in the In_6S_7 compound as the average oxidation state of In should be closer to In^{2+} than In^{3+}. Other possible origins could be related to distortions in the bonding distances, charge effects or quantum confinement, but they usually produce a global change in the core levels,[34] while shifts on the S (2p) core level are essentially negligible. Interestingly, the S-rich region of sample 1000A (S-1000A) shows In (3d) binding energies closer to samples 900B and 1000B than to the In_2S_3 reference powder. This seems to contradict the XRD results which indicated the presence of β-In_2S_3 on this region of sample 1000A. The energy difference between In($3d_{5/2}$) and S ($2p_{3/2}$) core levels is a better indication of the presence of different compounds as it is characteristic of each material and has the benefit of not being affected from external factors such as surface charging effects. The obtained values for the different samples are displayed in Table 1. Reference In_2S_3 powder has a value of In ($3d_{3/2}$) – S($2p_{3/2}$) = 283.2 eV, in agreement with reported values from the literature;[31] however, samples 900B, 1000B as well as S-1000A all show values of 283.5 eV, with no variation between them, further confirming the assignment to In_6S_7. The highly surface sensitive XPS technique confirms the presence of a very thin layer of In_6S_7 on the surface of samples 900A and S-1000A, which would explain their darker (gray or red) coloration as compared to the usual orange tone of the In_2S_3 powders. The corresponding diffraction intensity would be too weak to yield appreciable XRD peaks in a normal diffractometer, similar to what happened on sample 900B, where the XRD patterns were dominated by the underlying In_2O_3 even at grazing incidence conditions.

Representative O (1s) core level spectra recorded from samples 900B, 1000B, S-1000A and O-1000A are shown in Figure 6d. As mentioned before, all peaks can be fitted to a single component, which for sample O-1000A corresponds to the characteristic binding energy of oxygen bound to In^{3+} ions, as reported in the literature (BE O(1s) ~ 530.7 eV).[28,32] No traces of the characteristic signatures of oxygen deficient regions (BE O(1s) ~ 531.8 eV) or adsorbed oxygen (BE O(1s) ~ 532 eV) were found. Samples 900B, 1000B and S-1000A shows slightly larger binding energies, however, the observed shift is not large enough to be produced by adsorbed oxygen, and it is thus concluded that small amounts of O are incorporated into the In_6S_7 lattice (note that spectra in Figure 6d are normalized, the actual O (1s) intensities are much lower on these samples compared to the O-1000A one). The distinct crystalline environment with respect to In_2O_3 should account for the small BE differences compared to the sample O-1000A.

These results are consistent with the measured valence band profiles, shown in Figure 6e. As can be observed, the VB onset is shifted for samples 900B, 1000B and S-1000A (average E_F – VB ~ 1.26 eV) compared to reference In_2S_3 powders (E_F – VB ~ 1.68 eV) and sample O-1000A (E_F – VB ~ 2.15 eV). The last two values are compatible with slightly n-type In_2S_3 and In_2O_3, having bandgaps of 2.0 and 2.7 eV,[8,9,35] respectively. Oxygen vacancies in In_2O_3 are well known sources of charge carriers and the responsible for its intrinsic n-type doping. Therefore, the observed low doping level in sample O-1000A is in agreement with the absence of the O (1s) component at 531.8 eV, related to oxygen deficient regions. In_6S_7, on the other hand, is reported to have a direct band gap of approximately 0.9 eV.[22,23] Therefore the obtained E_F – VB values on samples 900B, 1000B and S-1000A would indicate a degenerate n-type state, with the Fermi level well within the conduction band. This degenerate doping could explain the metallic tone of the samples and its origin is most probably related to the presence of S vacancies (V_S), consistent with the attribution of the second component of the S (2p) core level to S deficient regions and the EDS results. Calculation of the relative

intensity between both S (2p) components could give an indication of the amount of V_S. However, the presence of O in the In_6S_7 can appear either as isoelectronic substitutional impurity, unaffecting the doping level, or in the form of O^{2-} interstitials, leading to compensating p-type doping, thus making the relation between the intensity ratio of both S (2p) components and the Fermi level non-trivial. On the other hand, incorporation of O leads to a widening in the bandgap of β-In_2S_3.[14] If a similar effect takes place on the In_6S_7 phase, it could partially explain the increased E_F – VB level observed in our samples. However, comparison of the intensity of the O (KVV) Auger peak relative to the In (4s) peak (Figure 6a) clearly indicates that the amount of O incorporated at the surface of this phase is significantly lower than in reference In_2S_3, and thus the expected effect of O into the In_6S_7 bandgap (if any) should be marginal.

The obtained morphologies and chemical compositions are clearly related to both the evaporation temperature of the precursor and the deposition temperature. An increased evaporation temperature leads to higher partial pressures of In and S in the furnace atmosphere, while a decreased temperature deposition enhances the rate at which both species can be incorporated onto the substrates. Hence, the formation of monoclinic In_6S_7 is favored at lower deposition temperatures (samples 900B and 1000B, 540 and 650 ºC respectively), while at higher deposition temperatures essentially β-In_2S_3 crystallites are obtained (samples 900A and S-1000A, 760 and 825 ºC, respectively), covered by a very thin In_6S_7 layer, only detectable by surface sensitive techniques (i.e. XPS). The fact that the edge of sample 1000B closer to the gas inlet, i.e. at slightly higher deposition temperature, is mainly covered by β-In_2S_3 while the rest of the sample is composed of In_6S_7 indicates that the temperature transition from favored deposition of In_6S_7 to β-In_2S_3 is close to 650 ºC. At deposition temperatures of 825 ºC or higher the formation of β-In_2S_3 is strongly inhibited, leading to almost uncovered substrates (sample 1000A). As the substrate temperature is reduced the amount of deposited In_2S_3 increases, changing the surface morphology from the early

formation of triangular grains and terraces (edge of sample 1000A, Figure 4a) to well-formed triangular crystals (sample 900A, Figure 3a), and columnar crystallites with 3-fold symmetry at lower deposition temperatures (edge of sample 1000B, Figure 4d). Since β-In_2S_3 is usually employed as buffer layer in solar cell applications, the formation of columnar crystallites could be used to enhance the capture of photogenerated carriers, similar to mesoporous TiO_2, and at the same time to reduce the sample reflectivity.

Comparison of XRD patterns recorded on samples 900B and 1000B, as well as the degree of coalescence of the nanowire bundles, indicate that the amount of In_6S_7 deposited on sample 1000B is far larger than on sample 900B, despite being at higher substrate temperature. This can be explained by the higher precursor temperature of the treatment at 1000 ºC, which leads to the evaporation of larger amounts of In and S, which are then available for the growth of In_6S_7 micro and nanostructures. Since the vapor pressure depends exponentially on the temperature, it is expected that the supersaturation increases more in the vicinity of sample 1000B than in sample 900B. Similarly, the anisotropic growth is usually enhanced by lower supersaturation values, which explains why the formation of nanowires and nanowire bundles is favored in sample 900B. The presence of a very thin In_6S_7 layer atop of the microstructured β-In_2S_3 crystallites appears as a rather interesting opportunity for solar cell applications as this process would directly combine an absorber (In_6S_7) and the In_2S_3 window/buffer layer.

4. Conclusion

In summary, we have successfully grown β-In_2S_3 columnar microcrystals and monoclinic In_6S_7 nanowires by a vapor phase deposition method, as confirmed by XRD and XPS. It was found that deposition of In_6S_7 is favored at temperatures below 650 ºC, while control of the supersaturation was possible by tuning the evaporation temperature, leading to the formation of either In_6S_7 nanowires or compact layers. At higher deposition temperatures the formation of β-In_2S_3 columnar microcrystals as well as compact layers is enhanced, while the growth of

In_6S_7 is limited to very thin layers atop. No traces of oxygen were found by EDS in the bulk of deposited In_6S_7 or In_2S_3 structures, and only minor incorporation of oxygen on the surface of the samples was detected by XPS. The formation of In_6S_7-In_2S_3 heterostructures seems as promising alternative for solar cell applications as both the absorber and window/buffer layers could be directly grown during the same treatment, with control on the morphology of the samples.

Acknowledgements

This work has been supported by MINECO/FEDER/M-ERA.net Cofund (Projects MAT2015-65274-R and PCIN-2017-106). J. B. acknowledges financial support from Universidad Complutense de Madrid. The authors thank M. Amatti and L. Gregoratti for their help during the XPS measurements and B. Sotillo for her help providing the furnace temperature profiles. Authors are fondly grateful to Prof. J. Piqueras as a dedicated mentor.

Received: ((will be filled in by the editorial staff))
Revised: ((will be filled in by the editorial staff))
Published online: ((will be filled in by the editorial staff))

References

[1] W. J. Duffin, J. H. C. Hogg, *Acta Crystallogr.* **1966**, *20*, 566.

[2] A. Y. Zavrazhnov, A. V. Kosyakov, A. V. Naumov, A. V. Sergeeva, S. S. Berezin, *Thermochim. Acta* **2013**, *566*, 169.

[3] B. Asenjo, A. M. Chaparro, M. T. Gutierrez, J. Herrero, J. Klaer, *Sol. Energy Mater. Sol. Cells* **2005**, *87*, 647.

[4] D. Braunger, D. Hariskos, T. Walter, H. W. Schock, *Sol. Energy Mater. Sol. Cells* **1996**, *40*, 97.

[5] J. F. Trigo, B. Asenjo, J. Herrero, M. T. Gutiérrez, *Sol. Energy Mater. Sol. Cells* **2008**, *92*, 1145.

[6] D. K. Nagesha, X. Liang, A. A. Mamedov, G. Gainer, M. A. Eastman, M. Giersig, J.-J. Song, T. Ni, N. A. Kotov, *J. Phys. Chem. B* **2001**, *105*, 7490.

[7] R. Diehl, R. Nitsche, *J. Cryst. Growth* **1975**, *28*, 306.

[8] N. Barreau, A. Mokrani, F. Couzinié-Devy, J. Kessler, *Thin Solid Films* **2009**, *517*, 2316.

[9] Z. Zhao, Y. Cao, J. Yi, X. He, C. Ma, J. Qiu, *ChemPhysChem* **2012**, *13*, 1551.

[10] M. F. Cansizoglu, R. Engelken, H.-W. Seo, T. Karabacak, *ACS Nano* **2010**, *4*, 733.

[11] T. T. John, S. Bini, Y. Kashiwaba, T. Abe, Y. Yasuhiro, C. S. Kartha, K. P. Vijayakumar, *Semicond. Sci. Technol.* **2003**, *18*, 491.

[12] S. Lugo-Loredo, Y. Peña-Méndez, M. Calixto-Rodriguez, S. Messina-Fernández, A. Alvarez-Gallegos, A. Vázquez-Dimas, T. Hernández-García, *Thin Solid Films* **2014**, *550*, 110.

[13] N. Barreau, J. C. Bernède, H. El Maliki, S. Marsillac, X. Castel, J. Pinel, *Solid State Commun.* **2002**, *122*, 445.

[14] N. Barreau, S. Marsillac, D. Albertini, J. C. Bernede, *Thin Solid Films* **2002**, *403–404*, 331.

[15] S. Yu, L. Shu, Y. Qian, Y. Xie, J. Yang, L. Yang, *Mater. Res. Bull.* **1998**, *33*, 717.

[16] W. Chen, J.-O. Bovin, A. G. Joly, S. Wang, F. Su, G. Li, *J. Phys. Chem. B* **2011**, *108*, 11927.

[17] M. Afzaal, M. A. Malik, P. O'Brien, *Chem. Commun.* **2004**, 334.

[18] C. Liang, Y. Shimizu, T. Sasaki, H. Umehara, N. Koshizaki, *J. Mater. Chem.* **2004**, *14*, 248.

[19] X. Xie, G. Shen, *Nanoscale* **2015**, *7*, 5046.

[20] J. H. C. Hogg, W. J. Duffin, *Acta Crystallogr.* **1967**, *23*, 111.

[21] G. A. Gamal, *Semicond. Sci. Technol.* **1997**, *12*, 1106.

[22] H. B. Abdallah, R. Bennaceur, *Phys. B (Amsterdam, Neth.)* **2006**, *382*, 181.

[23] C.-H. Ho, Y.-P. Wang, Y.-S. Huang, *Appl. Phys. Lett.* **2012**, *100*, 131905.

[24] T. Zdanowicz, T. Rodziewicz, M. Zabkowska-Waclawek, *Sol. Energy Mater. Sol. Cells* **2005**, *87*, 757.

[25] H. Daneshvar, R. Prinja, N. P. Kherani, *Appl. Energy* **2015**, *159*, 560.

[26] A. F. Qasrawi, N. M. Gasanly, *J. Phys.: Condens. Matter* **2006**, *18*, 4609.

[27] I.-H. Choi, S.-Y. Jang, H.-C. Kim, S. Huh, *Dalton Trans* **2018**, *47*, 1140.

[28] J. Bartolomé, D. Maestre, A. Cremades, M. Amatti, J. Piqueras, *Acta Mater.* **2013**, *61*, 1932.

[29] D. A. Magdas, A. Cremades, J. Piqueras, *Appl. Phys. Lett.* **2006**, *88*, 113107.

[30] J. Bartolomé, A. Cremades, J. Piqueras, *J. Mater. Chem. C* **2013**, *1*, 6790.

[31] Y. Tao, A. Yelon, E. Sacher, Z. H. Lu, M. J. Graham, *Appl. Phys. Lett.* **1998**, *60*, 2669.

[32] J. C. C. Fan, J. B. Goodenough, *J. Appl. Phys.* **1977**, *48*, 3524.

[33] "NIST X-ray Photoelectron Spectroscopy (XPS) Database, Version 3.5," can be found under https://srdata.nist.gov/xps/Default.aspx, **n.d.**

[34] S. W. Gaarenstroom, N. Winograd, *J. Chem. Phys.* **1977**, *67*, 3500.

[35] A. Walsh, J. L. F. Da Silva, S.-H. Wei, C. Körber, A. Klein, L. F. J. Piper, A. DeMasi, K. E. Smith, G. Panaccione, P. Torelli, D. J. Payne, A. Bourlange, R. G. Egdell, *Phys. Rev. Lett.* **2008**, *100*, 167402.

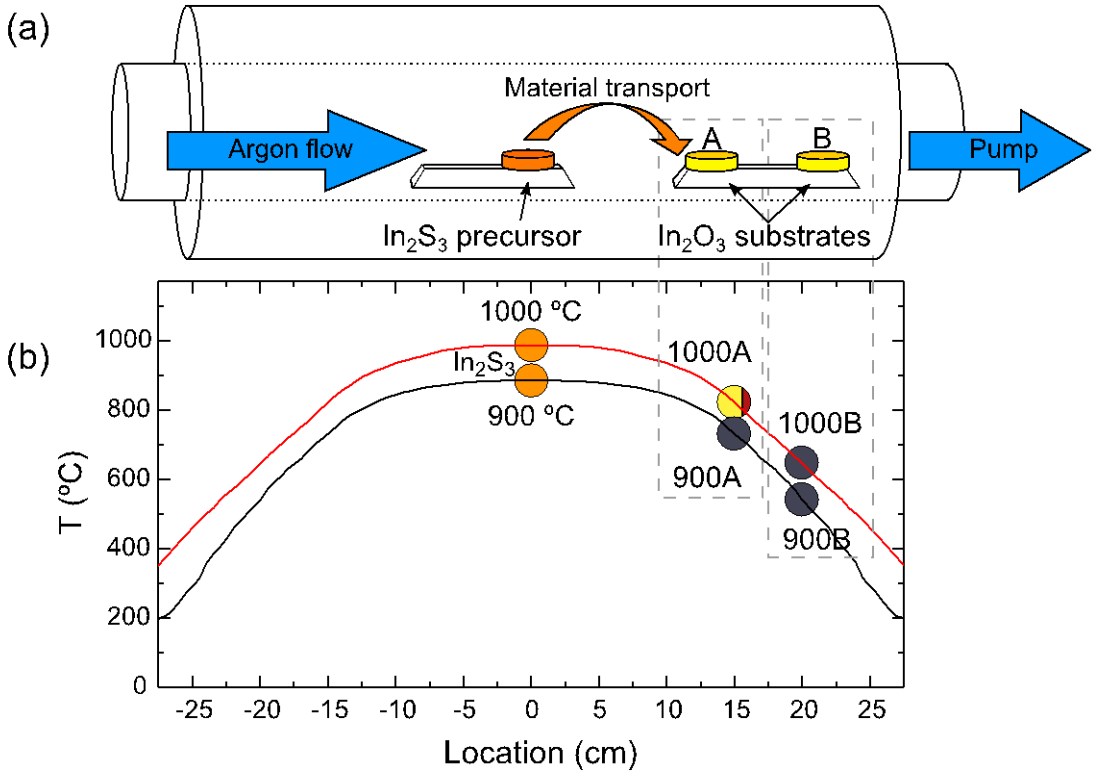

Figure 1. (a) Scheme of the experimental setup for the growth of the samples. (b) Temperature profile inside the furnace and location of the precursor and the substrates for each thermal treatment. Sample notation is indicated as a function of substrate thermal treatment and deposition temperature.

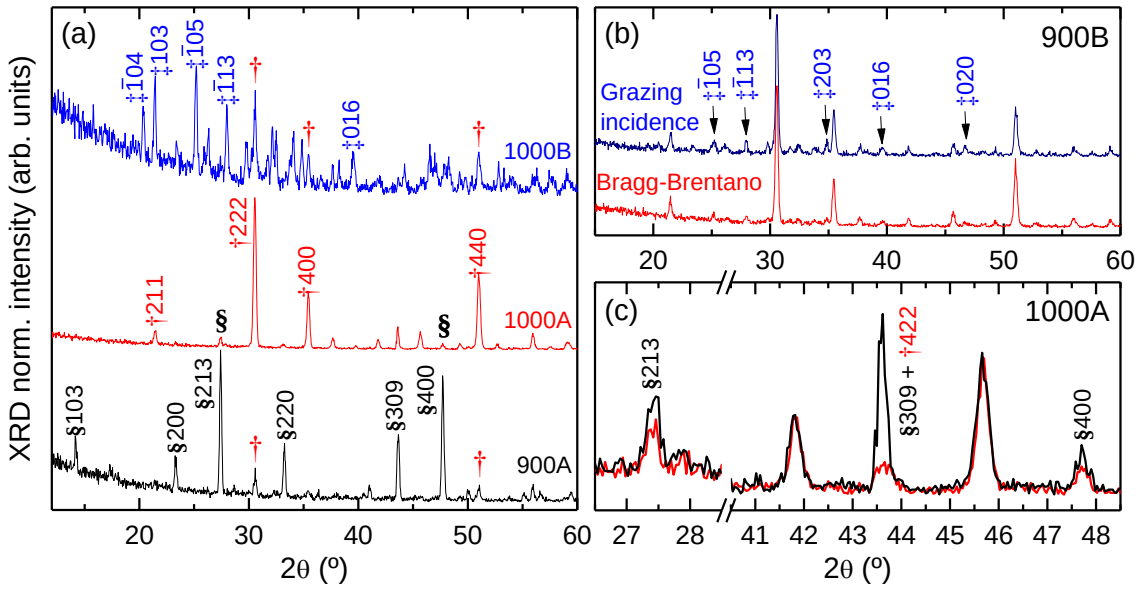

Figure 2. (a) Representative XRD patterns from samples 900A (In_2S_3, symbol §), 1000A (In_2O_3, symbol †) and 1000B (In_6S_7, symbol ‡). Some of the most intense peaks of each phase

are indexed. (b) The In_6S_7 layer in sample 900B is too thin to yield sufficiently intense diffraction peaks in Bragg-Brentano configuration, however, weak diffraction peaks from this phase are observed at grazing incidence. (c) Detail of the XRD patterns recorded at yellow (O-1000A, red line) and orange (S-1000A, black line) regions of sample 1000A, showing the increase in intensity of the weak In_2S_3 peaks when the orange region is located directly under the X ray beam.

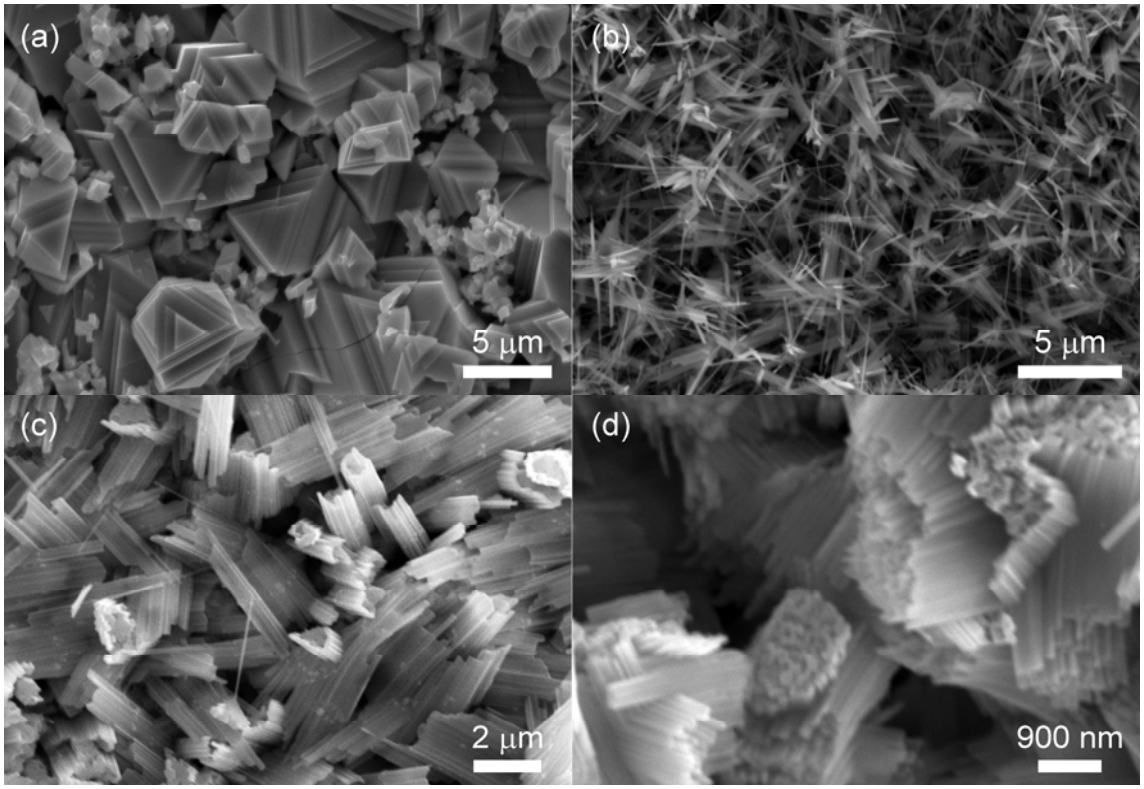

Figure 3. SEM images corresponding to the characteristic structures obtained at 900 ºC: (a) crystallites and triangular terraces of sample 900A. (b) and (c) a dense coverage of individual nanowires and nanowires bundles respectively from sample 900B. (d) A detail of the bundles in sample 900B.

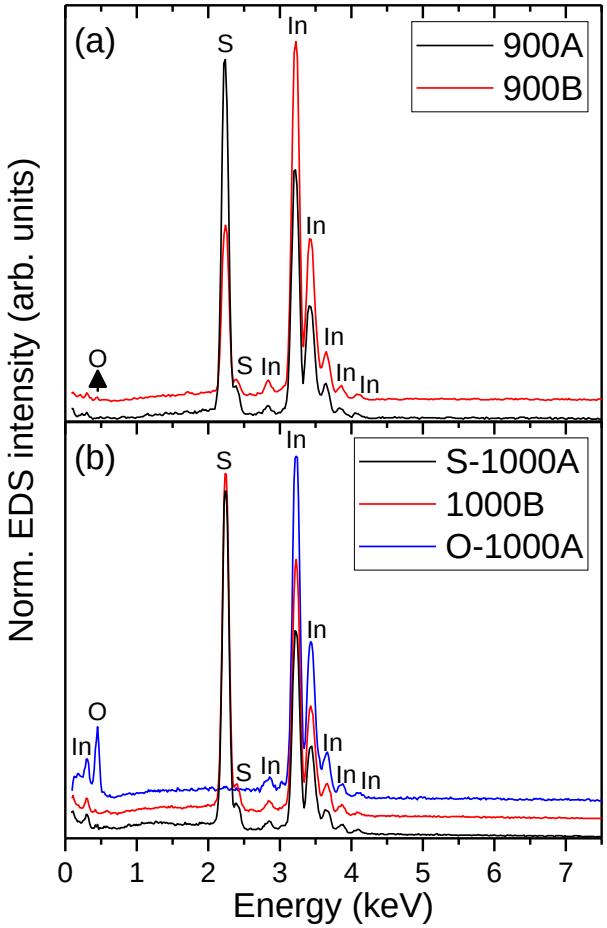

Figure 4. EDS spectra recorded on samples treated at (a) 900 ºC, substrates 900A (Figure 3a) and 900B (Figure 3b), and (b) 1000 ºC, substrates S-1000A (Figure 5a) O-1000A (inset of Figure 5a) and 1000B (Figure 5c). Arrow in (a) indicates the location of the O peak.

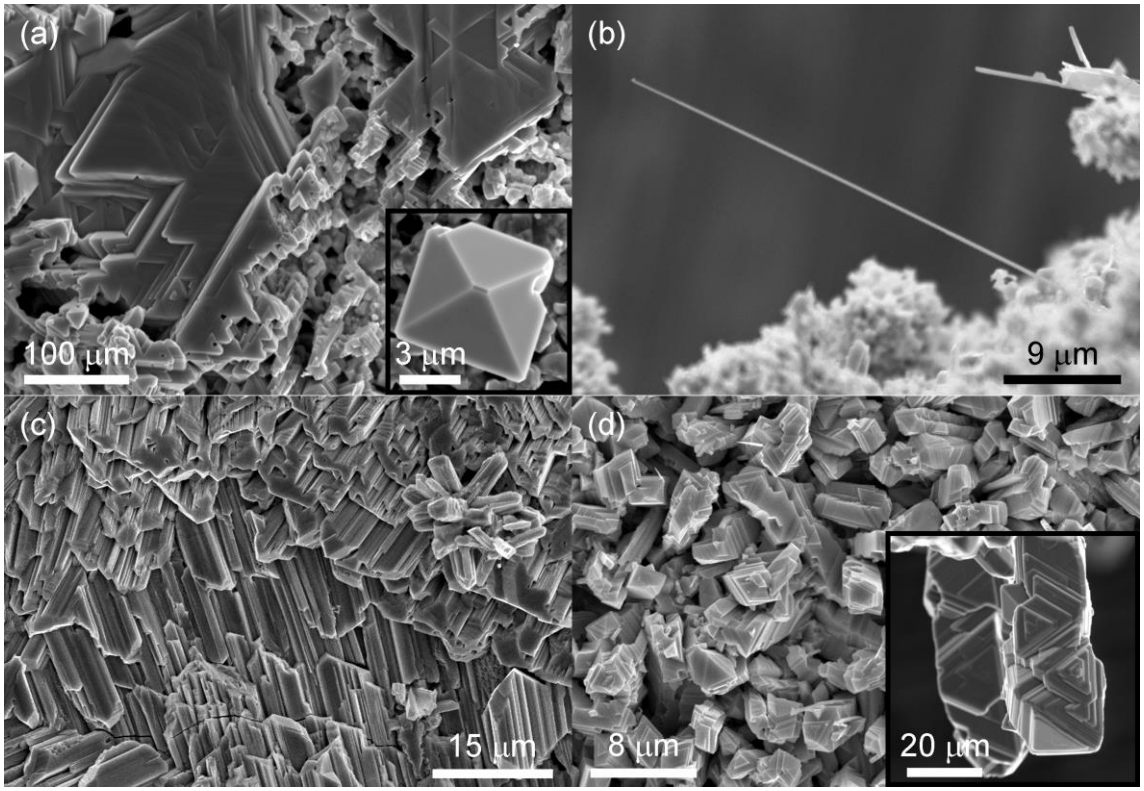

Figure 5. Representative SEM images of the structures obtained at 1000 ºC. (a) Coexistence of sintered In_2O_3 crystallites and triangular In_2S_3 grains and terraces from sample 1000A. Inset shows a well faceted In_2O_3 octahedron. (b) and (c) Example of an individual nanowire protruding from the edge of sample 1000B and elongated grains covering its surface. Elongated grains are formed from coalesced nanowire bundles. (d) Columnar crystallites obtained at the region closer to the gas inlet on sample 1000B. Inset in (d) shows a detail of two of these microcolumns.

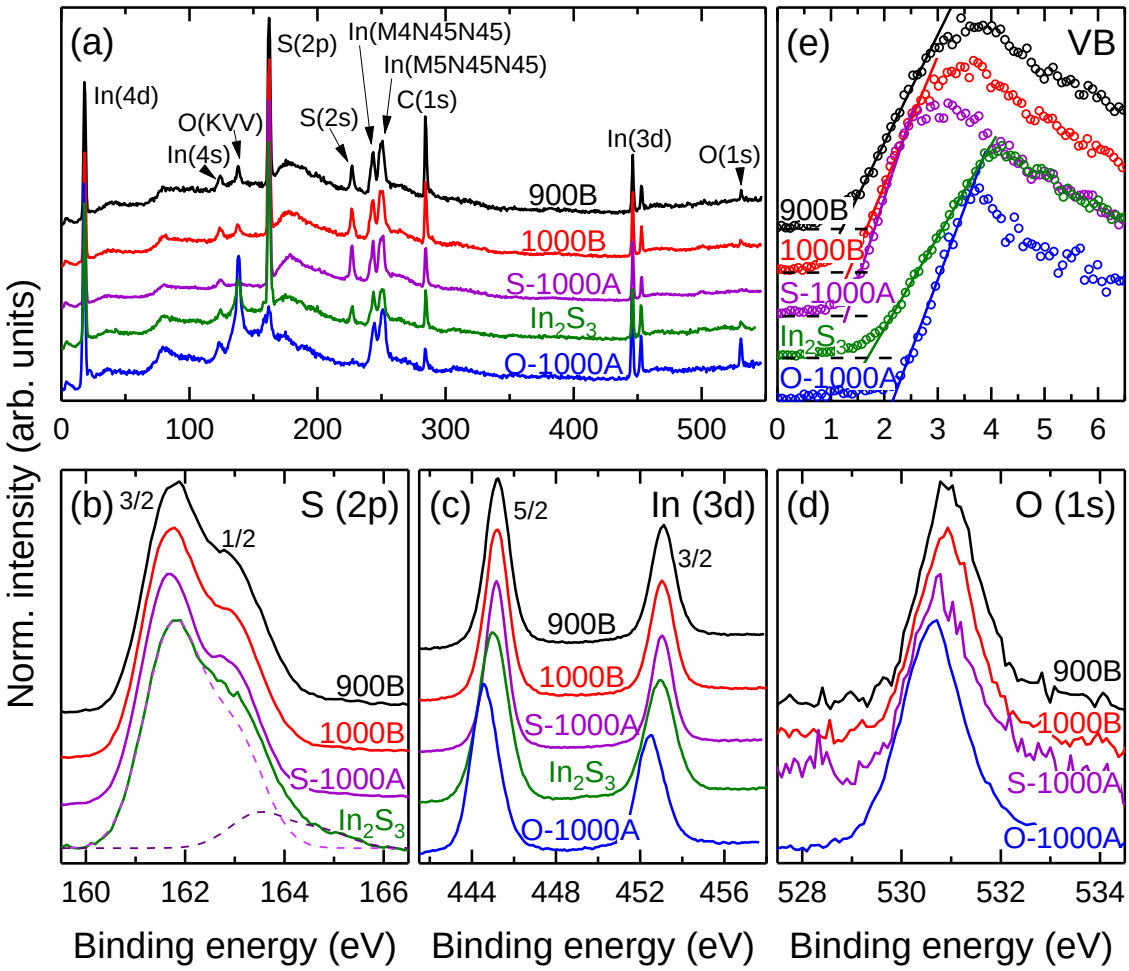

Figure 6. Representative normalized (a) XPS survey spectra, (b) S (2p), (c) In (3d), (d) O (1s) core levels and (e) VB region of the obtained phases, corresponding to the O and S rich regions of sample 1000A (O-1000A and S-1000A), the β-In_2S_3 precursor powders, and the In_6S_7 covered 900B and 1000B samples. The spectra are offset for the sake of clarity. Dashed lines in (b) are the best fit to two doublets of the S (2p) core level of reference In_2S_3 powders.

Table 1. Binding energies of the S (2p), In (3d) and O (1s) core levels as well as the energy of the Fermi level with respect to the valence band maximum (E_F – VB) for the studied samples. The energy difference between S($2p_{3/2}$) and In($3d_{5/2}$) is also indicated. All the values are given in eV.

Sample	S ($2p_{3/2}$)	S ($2p_{1/2}$)	In ($3d_{5/2}$)	In ($3d_{3/2}$)	O (1s)	E_F – VB	In ($3d_{5/2}$) – S ($2p_{3/2}$)
In_2S_3	161.75	163.01	444.99	452.93	-	1.68	283.2
900B	161.71	163.05	445.19	453.07	530.99	1.18	283.5
1000B	161.67	163.01	445.15	453.03	530.90	1.32	283.5
O-1000A	-	-	444.62	452.51	530.63	2.15	-
S-1000A	161.65	162.97	445.14	453.03	530.85	1.28	283.5